Science Advances
AAAS

Supplementary Materials for

Metallic *Mimosa pudica*: A 3D biomimetic buckling structure made of metallic glasses

Jin-Feng Li *et al.*

Corresponding author: Yong-Hao Sun, ysun58@iphy.ac.cn; Jiri Orava, jiri.orava@ujep.cz;
Hai-Yang Bai, hybai@iphy.ac.cn

Sci. Adv. **8**, eabm7658 (2022)
DOI: 10.1126/sciadv.abm7658

The PDF file includes:

Other Supplementary Material for this manuscript includes the following:

Supplementary Text

1. Laser parallel-line patterning

The *ns*-pulsed laser parallel-line scanning and the processing geometry are schematically illustrated in **fig. S1**, where *x*, *y*, *z* directions stand for length, width and thickness (*d*) of the ribbon, respectively, *s* refers to the laser line spacing (distance between centers of two laser lines), *w* is the laser linewidth. Patterning started from one corner of the ribbon, moved in a zigzag path, and ended in the opposite corner. The laser source was only ON while scanning the ribbon along the *x*-direction but OFF when moving from one line to another line. The procedure is termed parallel-line patterning.

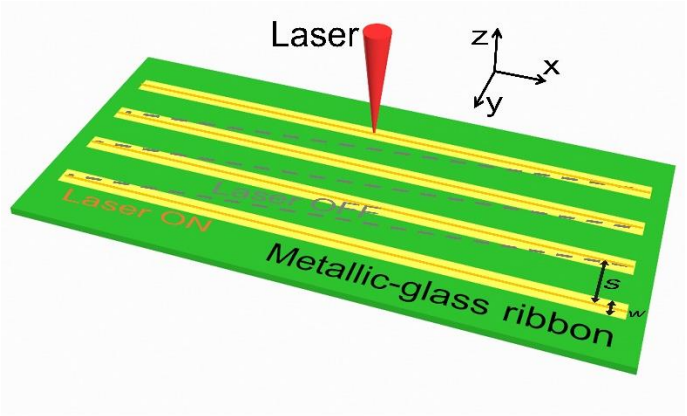

Fig. S1. Schematic of the parallel-line patterning.

The maximum temperature reached during laser patterning can be estimated by

using Dowden's model presented in *ref. 50*. A laser source is simplified as a point source at the surface of a semi-infinite workpiece. The maximum temperature (T_{max}) can be estimated according to:

$$T_{\max} = T_0 + \frac{P}{2\pi\lambda r}\exp\left\{\frac{v}{2\kappa}(x-r)\right\} \qquad \textbf{(S1)}$$

where the parameters are: T_0 – ambient temperature; P – incident power; λ – thermal conductivity; v – scanning speed; κ – thermal diffusivity; the origin is set as the central position of the laser spot; r the distance from any position in the sample to the origin; $x = r\cos\theta$; θ the angle of r to the x-direction. By taking P = 5 W (which counts for the influence of the reflectivity/absorption (50%) of MG and the percentage of power we applied), T_0 = 300 K, v = 0.1 m s^{-1}, r = 50 μm (half of the spot size), x = 50 μm, λ = 10.6 W m^{-1} K^{-1} and κ = 2.58 mm^2 s^{-1} (λ and κ of a similar MG composition, $Fe_{80}B_{20}$, are taken from *ref. 51*), then this gives T_{max} = 1802 K, which is above the melting temperature 1410 K, obtained independently by high-temperature calorimetry of $Fe_{78}Si_9B_{13}$ MG suggesting that the material was melted under the laser-scanning conditions for successful buckling.

2. Demonstration of the buckling

R of the naturally buckled roll is 10.75 mm, and of the reversed roll is 11.25 mm (**fig. S2)**. This difference in R can be explained by a small difference in w at the top and bottom surfaces: w at the bottom was about 5% smaller than that at the top surface, which is consistent with the previous observations (*52*). All the R given in the figures were measured for naturally buckled ribbons, i.e., immediately after laser-line

patterning.

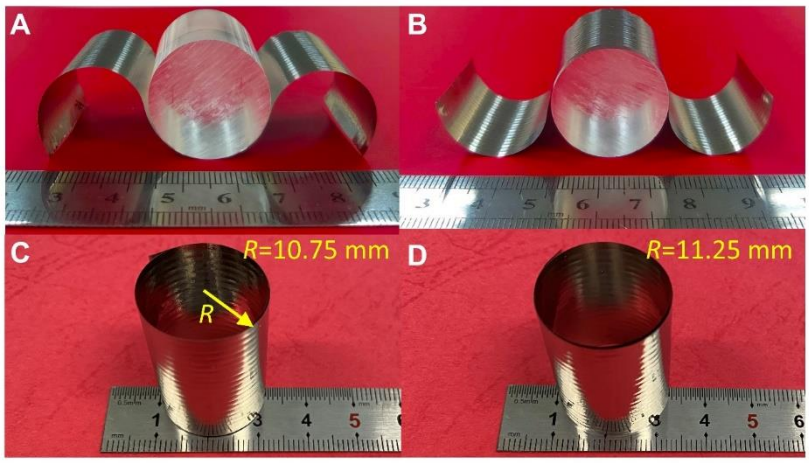

Fig. S2. Reversible 3D buckled structures (at *s* of 1.5 mm, *v* of 100 mm s^{-1}). (A) Concave and **(B)** convex geometries of the buckled ribbon; **(C)** Naturally buckled roll and **(D)** reversed roll. *R*: the curvature radius of MGC composite.

3. Analytical solution of *R* using the 2D model

The *R* of the buckled ribbon is determined by the energy minimum of the sum of bending and stretching energy (Equations 1, 2 & 3 in the manuscript). It includes 7 inputs, f_g, f_x, E_g, E_x, w_g, w_x, and d, and 3 variables, R, r_g and r_x. Here, f is the relative length change of the striped material, E the elastic modulus, w the linewidth, R the radius of curvature for the bulked structure along the laser lines direction, and r the radius of curvature for the modulated curves transverse to laser lines direction. In particular, f_x/f_g can be estimated by the density ratio between the two stripes, i.e., $f_x/f_g = (\rho_x/\rho_g)^{1/3}$; and $w_x = w$, $w_g = s - w$. For Fe-Si-B MG, w is 0.18 mm, s is 1.5 mm, d is 0.024 mm, E_g is 168.9 GPa, E_x is 217.8 GPa, ρ_g is 7.154 g cm^{-3}, and ρ_x is 7.375 g cm^{-3}. To obtain R corresponding to the minimum sum of energy, a MATLAB program "fmincon" is utilized to solve the multivariable (R, r_g and r_x) function (Eq. (1)-(3)),

together with the "multistart" solver for multiple local minima calculation. To see the trend of R vs. ρ_x/ρ_g, we fixed the E_x/E_g and w/s at default values and allowed ρ_x/ρ_g to change. For R vs. E_x/E_g and R vs. w/s, similar approaches were applied, too. The results are shown in **fig. S3**.

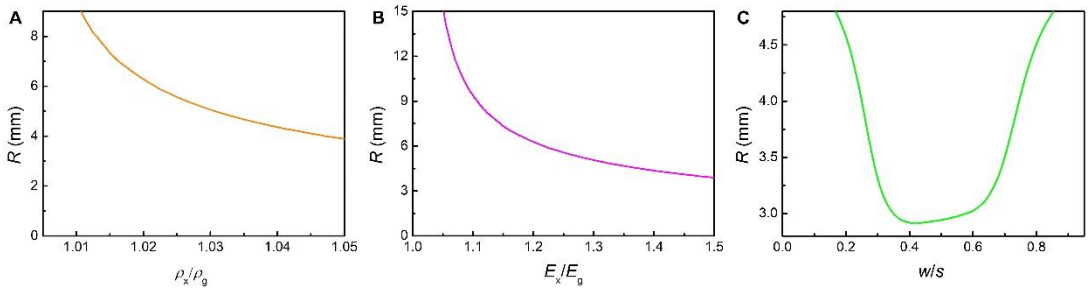

Fig. S3 The *R* is calculated by energy-minimum calculation. (A) R vs. ρ_x/ρ_g, **(B)** R vs. E_x/E_g, and **(C)** R vs. w/s.

From **fig. S3**, it can be seen that R decreases with increasing ρ_x/ρ_g and/or E_x/E_g; an optimum $w/s \sim 0.4$ exists corresponding to a minimum R (**fig. S3C**). While w/s is too large or too small the R goes to infinity, in these cases, buckling does not occur.

4. Kerr analysis

Fig. S4 demonstrates the evolution of magnetic domains upon the application of external tensile stress along the direction of the ribbon. In the stress-free state (**fig. S4A**), the ribbon had highly disordered domains governed by strongly varied local internal stresses. On applying external stress, the domains got more ordered and aligned along with the increasing stress principal (**fig. S4B to D**). The increasing ordering was accompanied by an increasing domains width. This kind of domains re-ordering were

expected due to the positive magnetostriction constant of the as-spun $Fe_{78}Si_9B_{13}$ ribbon.

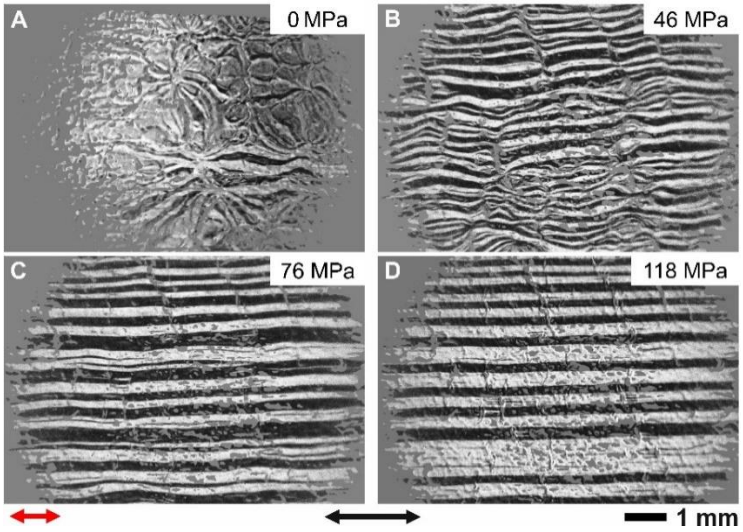

Fig. S4. Kerr microscopy overview of the magnetic domains on the surface of the as-spun $Fe_{78}Si_9B_{13}$ MG ribbon, part A, upon the application of increasing tensile stress along the ribbon axis, parts B-D, which agrees to *ref. 49*. The Kerr sensitivity is horizontal with the respect to the image plane (black arrow). The applied force, the direction is indicated by the red arrow and the tensile stress values are given in the labels, is oriented along the same axis.

The magnetic domains, shown in **fig. S5** in the as-spun state (A) and after successive laser patterning (B), demonstrates how far the stress propagates in the ribbon. The well-oriented in-plane wide domains induced by the tensile stress can be found as far as several millimeters away from the laser line.

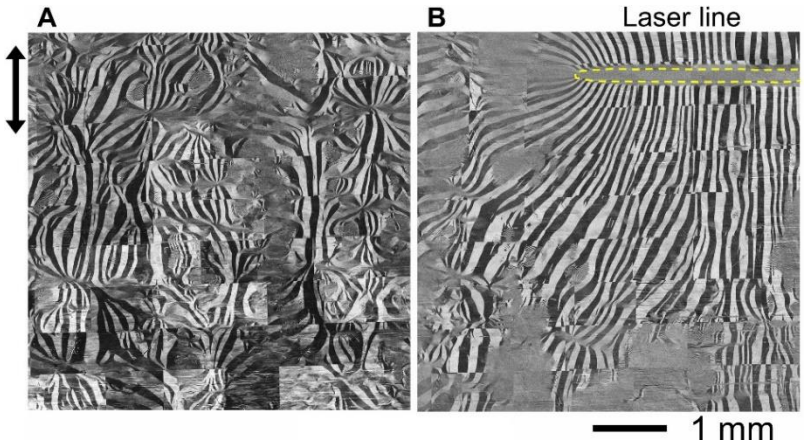

Fig. S5. The magnetic domains on the surface of $Fe_{78}Si_9B_{13}$ ribbon (v = 100 mm s^{-1}) contain a single laser line (enveloped by yellow dashed line). (A) As-spun ribbon, and **(B)** the ribbon after laser-patterning. The Kerr sensitivity is along the vertical direction (transverse to laser scanning) concerning the image plane (black arrow).

5. Experimental *R* of buckling structure

To further compare the extent of buckling, the curvature radius of composite structure (R) of the buckled ribbons was evaluated. Laser scanning speed v influences crystal stripe width w (**fig. S6**). R is a function of w and v (see **fig. S7)**. At a constant s of 2 mm, R increases with faster v from 40 to 120 mm s^{-1}. Similarly, at a constant v of 100 mm s^{-1}, the minimum spacing to obtain apparent buckling was 1.5 mm for R = 10 mm. R firstly increased with larger s and then leveled off at a constant value ~34 mm at s of about 10 mm. The R can be controlled by the ratio of w/s. Fig. 4F plots the dependence of R on the w/s ratio, and a universal correlation was observed. When w/s was higher than 25%, the ribbon buckled slightly due to the excessive penetration. Also, for w/s < 1%, buckling was not detected because the contribution of the crystalline part

is too small comparing with the line spacing. Therefore, for the ribbons of 24 μm thick used in this work, the achievable range of R is between 10–34 mm.

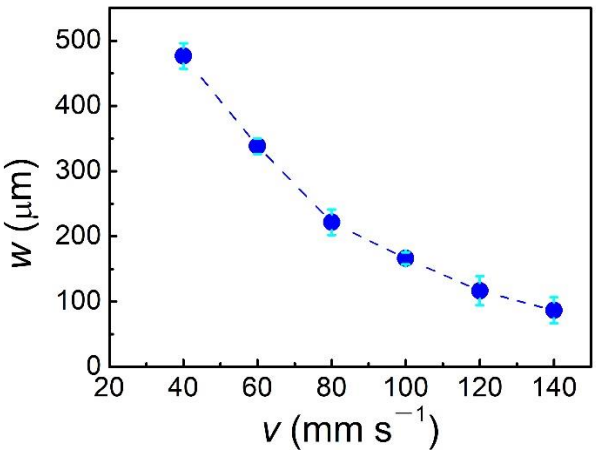

Fig. S6 *w* increases with decreasing *v*.

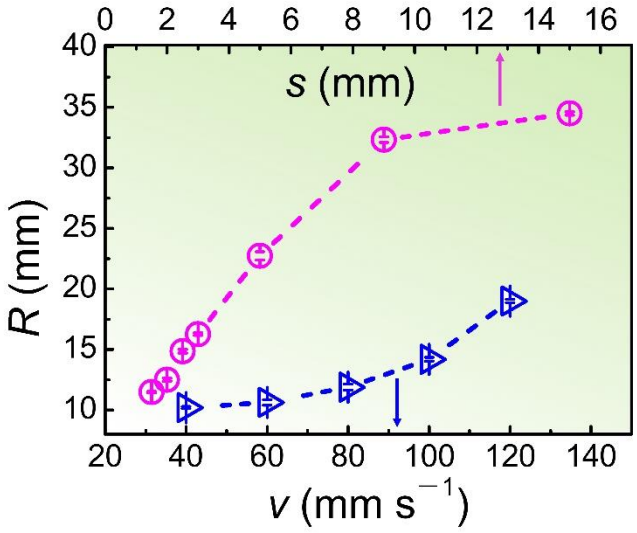

Fig. S7 *s* and *v* influences *R* of buckling structures.

Fig. S8 shows the 3D shape-change of $Fe_{78}Si_9B_{13}$ scanned ribbons after thermal annealing (5 min at 743-753 K). The ribbon was flattened after annealing, attributed to the removal of density difference between the relaxed glass and the crystallized regions.

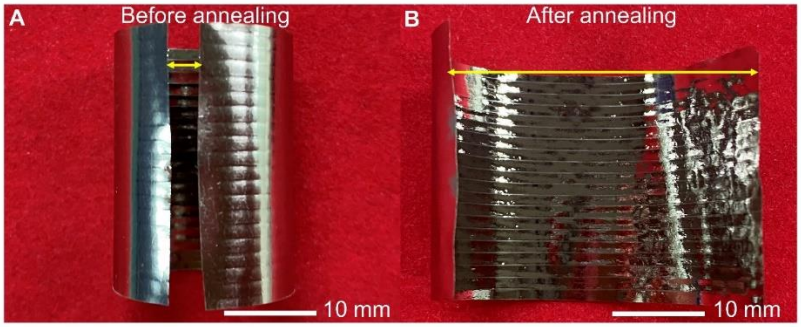

Fig. S8 Flattening of the buckled $Fe_{78}Si_9B_{13}$ ribbon after annealing. (A) As-spun ribbon via the laser patterning. **(B)** The buckled ribbon in (A) after thermal annealing (5 min at 743-753 K).

6. Structural and compositional characterizations of buckling ribbons

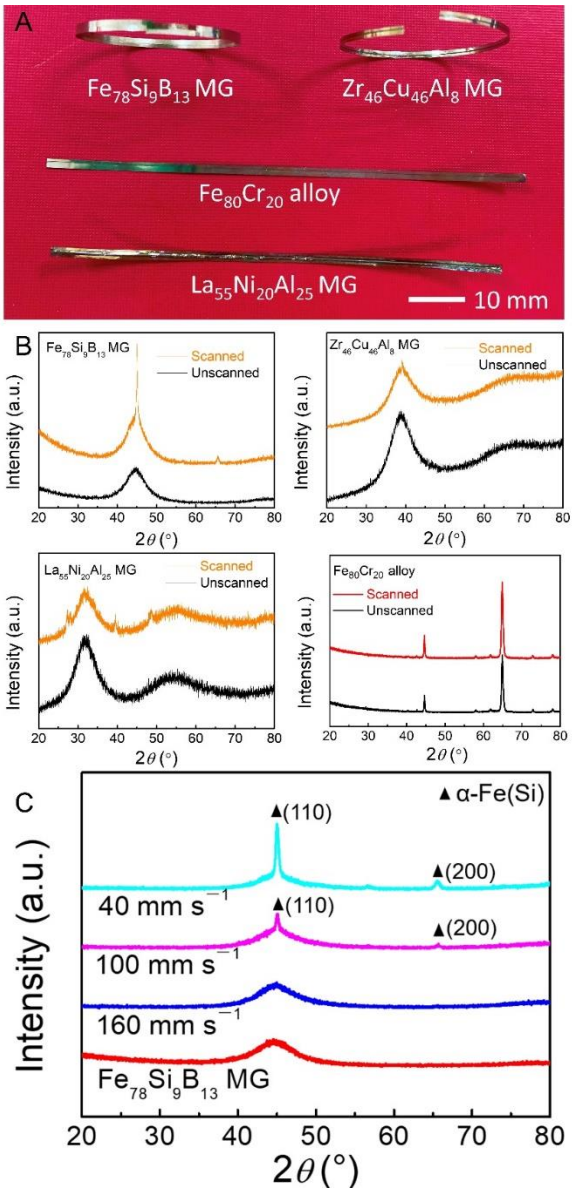

Fig. S9. Buckling of different composite ribbons. (A) Buckling shapes of $Fe_{78}Si_9B_{13}$, $Cu_{46}Zr_{46}Al_8$, $La_{55}Ni_{20}Al_{25}$ MGs and $Fe_{80}Cr_{20}$ polycrystal alloy ribbon after one-line laser patterning. The laser scanning speed v was set at 100 mm s^{-1}. **(B)** XRD of the laser scanned and unscanned ribbons. **(C)** XRD of as-spun and the laser scanned $Fe_{78}Si_9B_{13}$ ribbons at different v.

Fig. S9A shows the buckling structure of different ribbons after laser patterning of one line. $Fe_{78}Si_9B_{13}$ and $Cu_{46}Zr_{46}Al_8$ MGs show small R denoting evident buckling. But $La_{55}Ni_{20}Al_{25}$ MG and $Fe_{80}Cr_{20}$ polycrystal alloy show slightly buckling. **Table S1**

shows the density and elastic modulus change of $Fe_{78}Si_9B_{13}$, and $Zr_{46}Cu_{46}Al_8$ MGs before and after laser parallel-line processing. The successful buckling structure occurs in these two MGs, respectively. **Fig. S9B** presents the XRD patterns of the laser scanned and unscanned MG ribbons. Peaks of the crystallinities can be observed for all the samples after laser scanning. **Fig. S9C** shows the detected crystallinity of the buckled $Fe_{78}Si_9B_{13}$ ribbons. Taking the crystalline peak at 2θ = 44.96 ° for comparison, the size (D) of the crystals can be estimated by using the Scherrer equation, where $D = \frac{0.89\lambda_{XRD}}{B\cos\theta}$.

Because the wavelength of X-ray is 1.54 Å, θ is 22.48 °, and the full-width-half-maximum (B) is 0.345±0.023 ° for v = 100 mm s^{-1} and 0.377±0.008 ° for v = 40 mm s^{-1}, which gives D of 24.6±1.8 nm and 22.5±0.6 nm for v = 100 mm s^{-1} and 40 mm s^{-1}, respectively.

Fig. S10A shows slight buckling in $Fe_{78}Si_9B_{13}$ and $Cu_{46}Zr_{46}Al_8$ crystallized ribbon. The crystallized ribbons of the $Fe_{78}Si_9B_{13}$ and $Cu_{46}Zr_{46}Al_8$ before laser scanned are checked by XRD (**fig. S10B**) presenting polycrystal alloy, and then with one laser line post-scanned.

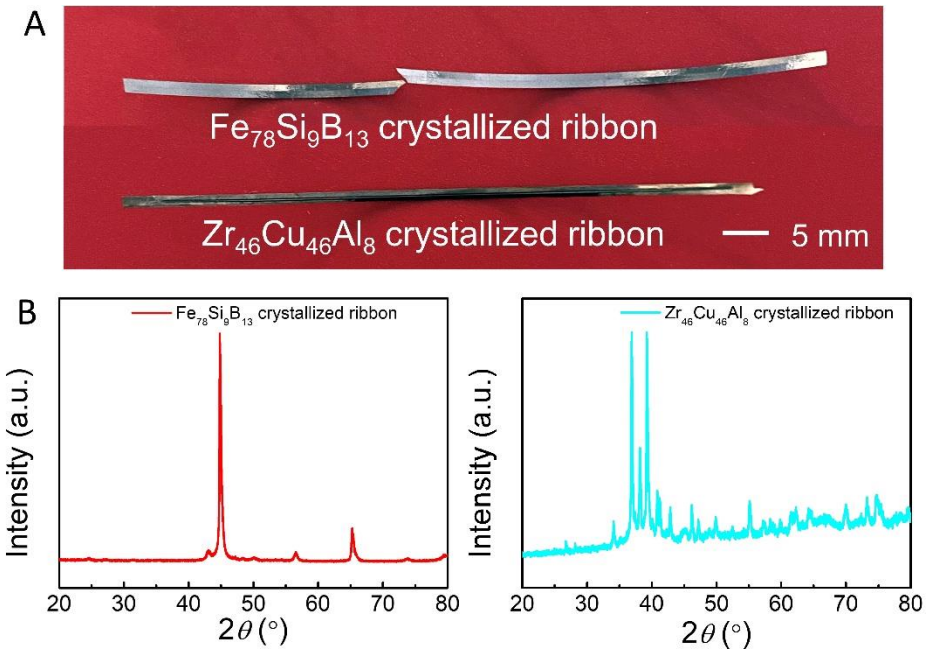

Figure S10 The slight buckling of the crystallized ribbon of $Fe_{78}Si_9B_{13}$ and $Zr_{46}Cu_{46}Al_8$ laser post-scanned. (A) Slight buckling of the crystallized ribbon. (B) The crystallized ribbon before laser scanned is examined by XRD.

Fig. S11 shows the SEM/EDS compositional maps of the laser-processed $Fe_{78}Si_9B_{13}$ MG ribbons. There is no detectable compositional difference between the MG matrix and the written line on the macroscopic length scale.

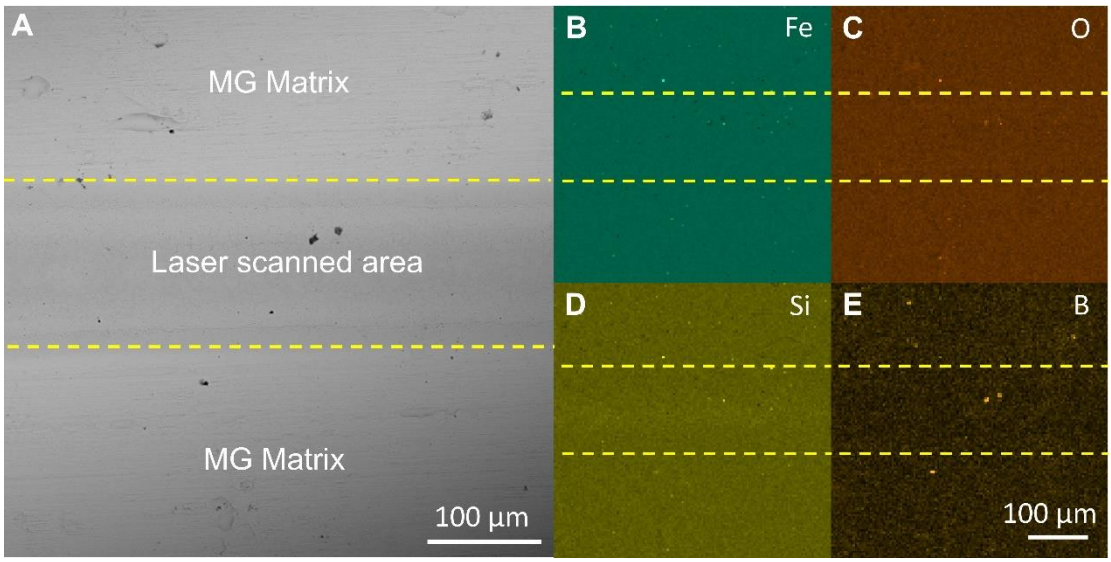

Fig. S11. Energy-dispersive X-ray analysis of the laser-processed $Fe_{78}Si_9B_{13}$ ribbon at v = 100 mm s^{-1}. (A) SEM image of the top surface. Concentration mapping of (B) iron, (C) oxygen, (D) silicon, and (E) boron.

Table S1 Density and elastic modulus change of $Fe_{78}Si_9B_{13}$, and $Zr_{46}Cu_{46}Al_8$ MGs before and after laser parallel-line processing.

Materials	ρ_g (g cm^{-3})	ρ_x (g cm^{-3})	ρ_x/ρ_g	E_g (GPa)	E_x (GPa)	E_x/E_g	Buckling
$Fe_{78}Si_9B_{13}$	7.154±0.003	7.375±0.003	1.031	168.9±3.7	217.8±10.8	1.29	Evident
$Zr_{46}Cu_{46}Al_8$	7.068±0.005	7.134±0.011	1.009	91.4±6.1	115.0±13.7	1.26	Evident

Movie S1 **Metallic mimosa pudica opens and closes upon the applied external magnetic field stimuli.** Metallic mimosa pudica opens and closes upon applied external magnetic field stimuli with various magnetic directions supplied by a magnet bar.

Movie S2 **The various postures of metallic mimosa pudica.** Seven convex and concave postures of the metallic petals are reshaped by manual.

Movie S3 **Comparison of responses of laser patterned and un-laser patterned petals upon applied magnetic field stimuli.** The laser patterned metallic mimosa pudica can open and close their petals upon magnetic stimuli easily, whereas the un-laser patterned petals can't do so.

Movie S4 **The laser patterning process.** The laser patterning process, the formation of 3D buckling structure of the Fe-based MG ribbon spontaneously, and easy rolling of the ribbon by manual.

REFERENCES AND NOTES

1. A. G. Volkov, J. C. Foster, T. A. Ashby, R. K. Walker, J. A. Johnson, V. S. Markin, Mimosa pudica: Electrical and mechanical stimulation of plant movements. *Plant Cell Environ.* **33**, 163–173 (2010).

2. J. Dervaux, M. B. Amar, Morphogenesis of growing soft tissues. *Phys. Rev. Lett.* **101**, 068101 (2008).

3. E. Sharon, B. Roman, M. Marder, G. S. Shin, H. L. Swinney, Buckling cascades in free sheets. *Nature* **419**, 579 (2002).

4. E. Sharon, M. Marder, H. L. Swinney, Leaves, flowers and garbage bags: Making waves. *Am. Sci.* **92**, 254–261 (2004).

5. X. Cheng, Y. Zhang, Micro/nanoscale 3D assembly by rolling, folding, curving, and buckling approaches. *Adv. Mater*. **31**, 1901895 (2019).

6. T. G. Leong, A. M. Zarafshar, D. H. Gracias, Three-dimensional fabrication at small size scales. *Small* **6**, 792–806 (2010).

7. N. Hu, R. Burgueño, Buckling-induced smart applications: Recent advances and trends. *Smart Mater. and Struct.* **24**, 063001 (2015).

8. M. Jamal, A. M. Zarafshar, D. H. Gracias, Differentially photo-crosslinked polymers enable self-assembling microfluidics. *Nat. Commun.* **2**, 527 (2011).

9. J. Y. Chung, A. J. Nolte, C. M. Stafford, Surface wrinkling: A versatile platform for measuring thin-film properties. *Adv. Mater.* **23**, 349–368 (2011).

10. Z. Liu, A. Cui, J. Li, C. Gu, Folding 2D structures into 3D configurations at the micro/nanoscale: Principles, techniques, and applications. *Adv. Mater.* **31**, 1802211 (2019).

11. T. van Manen, S. Janbaz, A. A. Zadpoor, Programming the shape-shifting of flat soft matter. *Mater. Today* **21**, 144–163 (2018).

12. A. S. Gladman, E. A. Matsumoto, R. G. Nuzzo, L. Mahadevan, J. A. Lewis, Biomimetic 4D printing. *Nat. Mater.* **15**, 413–418 (2016).

13. R. M. Erb, J. S. Sander, R. Grisch, A. R. Studart, Self-shaping composites with programmable bioinspired microstructures. *Nat. Commun.* **4**, 1712 (2013).

14. Z. L. Wu, M. Moshe, J. Greener, H. Therien-Aubin, Z. Nie, E. Sharon, E. Kumacheva, Three-dimensional shape transformations of hydrogel sheets induced by small-scale modulation of internal stresses. *Nat. Commun.* **4**, 1586 (2013).

15. C. Ohm, M. Brehmer, R. Zentel, Liquid crystalline elastomers as actuators and sensors. *Adv. Mater.* **22**, 3366–3387 (2010).

16. E. A. Peraza-Hernandez, D. J. Hartl, R. J. Malak Jr., D. C. Lagoudas, Origami-inspired active structures: A synthesis and review. *Smart Mater. Struct.* **23**, 094001 (2014).

17. G. Stoychev, S. Turcaud, J. W. C. Dunlop, L. Ionov, Hierarchical multi-step folding of polymer bilayers. *Adv. Funct. Mater.* **23**, 2295–2300 (2013).

18. N. Lazarus, G. L. Smith, M. D. Dickey, Self-folding metal origami. *Adv. Intell. Syst.* **1**, 1900059 (2019).

19. N. Lazarus, A. A. Wilson, G. L. Smith, Contactless laser fabrication and propulsion of freely moving structures. *Extreme Mech. Lett.* **20**, 46–50 (2018).

20. N. Lazarus, G. L. Smith, Laser folding in a roll-to-roll manufacturing process. *Lasers Manuf. Mater. Process.* **5**, 237–247 (2018).

21. N. Lazarus, S. S. Bedair, G. L. Smith, Origami inductors: Rapid folding of 3D coils on a laser cutter. *IEEE Electron Device Lett.* **39**, 1046–1049 (2018).

22. X. Ning, X. Yu, H. Wang, R. Sun, R. E. Corman, H. Li, C. M. Lee, Y. Xue, A. Chempakasseril, Y. Yao, Z. Zhang, H. Luan, Z. Wang, W. Xia, X. Feng, R. H. Ewoldt, Y. Huang, Y. Zhang, J. A. Rogers, Mechanically active materials in three-dimensional mesostructures. *Sci. Adv.* **4**, eaat8313 (2018).

23. 16. D. Rus, M. T. Tolley, Design, fabrication and control of origami robots. *Nat. Rev. Mater.* **3**, 101–112 (2018).

24. X. Wang, G. Mao, J. Ge, M. Drack, G. S. C. Bermúdez, D. Wirthl, R. Illing, T. Kosub, L. Bischoff, C. Wang, J. Fassbender, M. Kaltenbrunner, D. Makarov, Untethered and ultrafast soft-bodied robots. *Commun. Mater.* **1**, 67 (2020).

25. Y. Kim, H. Yuk, R. Zhao, S. A. Chester, X. Zhao, Printing ferromagnetic domains for untethered fast-transforming soft materials. *Nature* **558**, 274–279 (2018).

26. C. L. Randall, E. Gultepe, D. H. Gracias, Self-folding devices and materials for biomedical applications. *Trends Biotechnol.* **30**, 138–146 (2012).

27. D. Pohl, W. D. Wolpert, Engineered spacecraft deployables influenced by nature. *Proc. SPIE* **7424**, 742408 (2009).

28. A. L. Greer, Metallic glasses. *Science* **267**, 1947–1953 (1995).

29. J. F. Löffler, Bulk metallic glasses. *Intermetallics* **11,** 529–540 (2003).

30. W. H. Wang, C. Dong, C. H. Shek, Bulk metallic glasses. *Mater. Sci. Eng. R* **44**, 45–89 (2004).

31. Y. Li, Q. Guo, J. A. Kalb, C. V. Thompson, Matching glass-forming ability with the density of the amorphous phase. *Science* **322**, 1816–1819 (2008).

32. W. H. Wang, The elastic properties, elastic models and elastic perspectives of metallic glasses. *Prog. Mater. Sci.* **57**, 487–656 (2012).

33. C. Zhang, X.-M. Li, S.-Q. Liu, H. Liu, L.-J. Yu, L. Liu, 3D printing of Zr-based bulk metallic glasses and components for potential biomedical applications. *J. Non Cryst. Solids* **790**, 963–973 (2019).

34. M. Aljerf, K. Georgarakis, A. R. Yavari, Shaping of metallic glasses by stress-annealing without thermal embrittlement. *Acta Mater.* **59**, 3817–3824 (2011).

35. H. Xian, M. Liu, X. Wang, F. Ye, P. Wen, H. Bai, Y. Liu, W. Wang, Flexible and stretchable metallic glass micro- and nano-structures of tunable properties. *Nanotechnology* **30**, 085705 (2019).

36. N. T. Panagiotopoulos, K. Georgarakis, A. M. Jorge Jr., M. Aljerf, W. J. Botta, A. R. Yavari, Advanced ultra-light multifunctional metallic-glass wave springs. *Mater. Des.* **192**, 108770 (2020).

37. Z. Liu, W. Chen, J. Carstensen, J. Ketkaew, R. M. Ojeda Mota, J. K. Guest, J. Schroers, 3D metallic glass cellular structures. *Acta Mater.* **105**, 35–43 (2016).

38. J. V. Carstensen, R. Lotfi, W. Chen, S. Szyniszewski, S. Gaitanaros, J. Schroers, J. K. Guest, Topology-optimized bulk metallic glass cellular materials for energy absorption. *Scr. Mater.* **208**, 114361 (2022).

39. N. T. Panagiotopoulos, M. A. Yousfi, K. Georgarakis, A. R. Yavari, Mechanically induced waves in metallic glass foils. *Mater. and Des.* **90**, 1110–1114 (2016).

40. G. Kaltenboeck, M. D. Demetriou, S. Roberts, W. L. Johnson, Shaping metallic glasses by electromagnetic pulsing. *Nat. Commun.* **7**, 10576 (2016).

41. E. Sharon, E. Efrati, The mechanics of non-Euclidean plates. *Soft Matter* **6**, 5693–5704 (2010).

42. I. V. Soldatov, J. Zehner, K. Leistner, T. Kang, D. Karnaushenko and R. Schafer, Advanced, Kerr-microscopy-based MOKE magnetometry for the anisotropy characterisation of magnetic films. *J. Magn. Magn. Mater.* **529**, 167889 (2021).

43. A. Hubert, R. Schäfer, *Magnetic Domains: The Analysis of Magnetic Microstructures* (Springer Berlin Heidelberg, 1998).

44. E. Lopatina, I. Soldatov, V. Budinsky, M. Marsilius, L. Schultz, G. Herzer, R. Schäfer, Surface crystallization and magnetic properties of $Fe_{84.3}Cu_{0.7}Si_4B_8P_3$ soft magnetic ribbons. *Acta Mater.* **96**, 10–17 (2015).

45. R. Hilzinger, W. Rodewald, *Magnetic Materials: Fundamentals, Products, Properties, Applications* (Wiley, 2013).

46. C. Zhang, Y. Dong, C. Ye, Recent developments and novel applications of laser shock peening: A review. *Adv. Eng. Mater.* **23**, 2001216 (2021).

47. B. Chen, Y. Li, M. Yi, R. Li, S. Pang, H. Wang, T. Zhang, Optimization of mechanical properties of bulk metallic glasses by residual stress adjustment using laser surface melting, *Scr. Mater.* **66**, 1057–1060 (2012).

48. I. V. Soldatov, R. Schäfer, Selective sensitivity in Kerr microscopy. *Rev. Sci. Instrum.* **88**, 073701 (2017).

49. R. Schäfer, I. V. Soldatov, S. Arai, Power frequency domain imaging on Goss-textured electrical

steel, *J. Magn. Magn. Mater.* **474**, 221–235 (2019).

50. J. M. Dowden, *The Mathematics of Thermal Modeling: An Introduction to the Theory of Laser Material Processing* (Chapman & Hall/CRC USA, 2001).

51. U. Harms, T. D. Shen, R. B. Schwarz, Thermal conductivity of $Pd_{40}Ni_{40-x}Cu_xP_{20}$ metallic glass. *Scripta Mater.* **41**, 411–414 (2002).

52. J. F. Li, Y. H. Sun, W. D. Ding, W. H. Wang, H. Y. Bai, Nanosecond-pulsed laser welding of metallic glass. *J. Non Cryst. Solids*, **537**, 120016 (2020).